

ORIGINAL RESEARCH ARTICLE

Increasing density and mechanical performance of binder jetting processing through bimodal particle size distribution

Ana Paula Clares¹, Yawei Gao², Ryan Stebbins², Adri C.T. van Duin²,
Guha Manogharan^{1,2*}

¹Additive Manufacturing and Design Graduate Program, The Pennsylvania State University, University Park, PA 16801, USA

²Department of Mechanical Engineering, The Pennsylvania State University, University Park, PA 16801, USA

Abstract

Binder jetting is an additive manufacturing (AM) technology that has gained popularity and attention in recent years for production applications in tooling, biomedical, energy, and defense sectors. When compared to other powder bed fusion-based AM methods, binder jetting processes powder feedstock without the need of an energy source during printing. This avoids defects associated with melting, residual stresses, and rapid solidification within the parts. However, one of the challenges of this process is the relatively lower densities which impacts part density, and subsequently, sintering and mechanical properties. In this study, we investigated the influence of bimodal powder size distributions (a mixture of coarse to fine particles) as a method for increasing part density and mechanical strength, and used stainless steel (SS) 316L bimodal mixtures in this case. Four unimodal and two bimodal groups were evaluated under similar AM processing conditions for sintered density measurements and flexural strengths. Our results demonstrated that bimodal size distributions showed a statistically significant increase in density by 20% and ultimate flexural strength by 170% when compared to the highest performing unimodal group. In addition to experimental findings, reactive molecular dynamics simulations showed that the presence of finer powders along with coarser particles in the bimodal particle mixture contribute to additional bonds that are stronger across the particle interfaces. Findings from this study can be used to design bimodal particle size distributions to achieve higher density and better mechanical properties in binder jetting AM process.

***Corresponding author:**

Guha Manogharan
(gum53@psu.edu)

Citation: Clares AP, Gao Y, Stebbins R, *et al.*, 2022, Increasing density and mechanical performance of binder jetting processing through bimodal particle size distribution. *Mater Sci Add Manuf*, 1(3): 20
<https://doi.org/10.18063/msam.v1i3.20>

Received: August 26, 2022

Accepted: September 15, 2022

Published Online: September 29, 2022

Copyright: © 2022 Author(s). This is an Open Access article distributed under the terms of the Creative Commons Attribution License, permitting distribution, and reproduction in any medium, provided the original work is properly cited.

Publisher's Note: Whioce Publishing remains neutral with regard to jurisdictional claims in published maps and institutional affiliations.

Keywords: Binder jetting; Bimodal powder; Mechanical strength; Molecular dynamics; 316L stainless steel; Additive manufacturing

1. Introduction

Binder jetting was developed in the early 1990s and is one of the seven additive manufacturing (AM) technologies. Similar to direct energy deposition (DED) and laser powder bed fusion (LPBF), this technology processes powder feedstock for the fabrication of parts. The process begins with powder dispensing with a rake or blade or rotating roller to spread a thin layer of powder on a build platform. Next, the binder

is selectively deposited with an array of nozzles that eject the solution onto the powder bed. This process is repeated layer by layer until a final part is achieved to produce a “green part.” On build completion, post-processing steps, such as curing, depowering, sintering, infiltration, and finishing, are necessary to achieve final densification.

Binder jetting offers multiple advantages, such as eliminating the need for support structures, powder reusability, and part nesting. In contrast to other powder AM technologies, it is a non-fusion-based process that does not rely on high energy sources (e.g., laser and electron beam) during fabrication. The only external heat present during the process is for the partial drying of the binder across each layer. The lack of elevated heat input is beneficial as it evades melting and rapid solidification defects, as well as residual stresses accumulated in other AM processed parts^[1]. Binder jetting is regarded as a very flexible AM technique that offers a wide range of material selections, such as sand, ceramics, polymers, and metals^[1]. Applications of binder jetting include tooling, fuel cells, scaffolds, molds, construction, and electronic antenna^[2-11] due to its ability in fabricating relatively complex geometries rapidly at larger volumes, and lower machine and production costs^[12]. The lack of distortions introduced to the part due to the absence of thermal gradients, and the lack of thermal crack formations makes this AM technology attractive for continuous investigation in academia and industrial applications. When compared to LPBF and DED, the number of materials investigated in binder jetting is smaller but that is increasing^[13].

Despite the high popularity of binder jetting, especially for optically reflective and thermally conductive metals^[14], one of its limitations is the relatively lower densities of printed parts when compared to fabrications through powder metallurgy or other metal AM processes^[15]. Binder jetting as-built (green stage) parts are typically brittle, porous, and with lower mechanical properties^[16]. The previous work reported average relative densities obtained of around 40 – 60% in binder jetting fabrications^[16-18]. Efforts have been made to increase the overall density of printed part in post-processing, such as infiltration, hot isostatic pressing (HIP), optimization of printing process parameters, and powder properties^[15]. For example, Vogt *et al.* reported a 26% increase in green density after infiltration^[19] while Porter *et al.* calculated a 65% density improvement when compared to green parts during the fabrication of Al-based metal matrix nanocomposites^[20]. Kumar *et al.* demonstrated that through the use of the HIP technique, a maximum density of 97% and 92% in copper parts could be achieved^[21,22]. Another study showed that full densification was achieved with HIP in binder jetting of nickel-based superalloy^[23]. Optimization process parameters have also been studied for density improvement. Shrestha *et*

al. analyzed the impact of several process parameters (binder saturation, layer thickness, and feed-to-powder ratio) and concluded that achieving higher packing density during powder spreading is critical to achieving higher final density^[24]. Lecis *et al.* also studied the influence of layer thickness, binder saturation, as well as debinding and sintering atmospheres to achieve final densities of 98%^[12].

The focus of this work lies in the effects of powder properties, specifically powder size distribution during binder jetting to achieve superior part properties through higher density. Prior efforts in powder metallurgy have shown that bimodal powder mixtures can improve packing density and dimensional control after sintering^[14,25]. Both coarse and fine particles are mixed (e.g., 1:3-1:6 volumetric ratios) to increase packing density through filling of fine particles into the voids created between the coarse particles^[26]. Du *et al.* investigated the use of bimodal powder feedstocks in silicon carbide ceramics by achieving a 5% increase in green density when compared to unimodal powder prints^[25]. Du *et al.* used spherical alumina powders to demonstrate the improvements in powder bed density and sintered density with an analytical model to find the optimal mixing fraction in bimodal mixtures^[27]. Bai *et al.* experimentally evaluated the effect of bimodal copper printed parts and observed an increase of 16.2% in powder bed density and 12.3% in sintered density, depending on the variation of sinter conditions^[15]. Bai *et al.* studied the impact of copper bimodal mixtures that resulted in an 8.2% improvement in powder packing density and a 4% increase in sintered density^[19]. Sinterability and density improvements were also observed in bimodal size distribution in binder jetting of SS 316L but its effects on mechanical strength were not evaluated^[20].

Even though the impact of bimodal distributions in green and sintered densities has been explored, there is still a need to understand the effect of bimodal particle size distribution in SS316L binder jetting and its impact on sintered density and mechanical performance. The motivation of this paper is to experimentally validate the benefits of bimodal mixtures on sintered density and mechanical performance. This effort builds on a previous computational work based on discrete element method and the effects of particle size distributions on packing density, porosity, and flowability^[28]. In addition, the experimental work of this paper serves as a benchmark for the modeling work, which provides an atomistic level insight into the strengthening mechanism of the bimodal particle size distribution using the ReaxFF molecular dynamics (MD) simulations.

Section 2 describes the experimental methods with a focus on material selection, powder characterization, part fabrication and printing conditions, as well as post-

processing. Section 3 describes the characterization and evaluation techniques employed in this study. Sections 4 and 5 detail the results obtained in this study and discuss their implications, respectively. Finally, Section 6 highlights the major findings and directions for future research.

2. Experimental methods

2.1. Material selection

Nitrogen gas atomized (SS316L) 316L stainless steel powder with similar chemical compositions were obtained from two powder manufacturers, Sandvik (Stockholm, SE) and Carpenter Additive (Philadelphia, USA). Batch sampling was conducted using ELEMENTRAC ONH-p 2 and ELEMENTRAC CS-1 (ELTRA, USA) for total C, S, O, N, and H content. The O%, N%, and H% content were extracted through inert gas fusion technique, while combustion was used for C% and S% concentration (Table 1).

2.2. Powder characterization

To evaluate the impact of powder size distribution, six powder size groups were prepared using a vibratory sieve (Retsch AS 200 Control, Haan DE), as shown in Table 2 for four unimodal and two bimodal distributions.

Using dynamic image analysis (DIA) technique through Microtrac MRB-CAMSIZER X2 equipment (Newtown, PA), particle size distribution and morphology were measured following the ISO 13322-2 standard^[29]. As shown in Figure 1A, median particle size (D50) values for unimodal groups are around 12 μm , 22 μm , 31 μm , and 36 μm for Groups 1, 2, 3, and 4, respectively. Groups 5 and 6 consist of bimodal particle size distributions, which is a combination of coarse and fine particles. Based on literature work, a coarse fine particle size ratio of 1:3 – 1:4 is ideal

Table 1. Chemical composition of as sourced SS316L powders

Powder manufacturer	C%	S%	O%	N%	H (ppm)
Carpenter Additive	0.014	0.005	0.040	0.090	5.490
Sandvik Osprey	0.013	0.004	0.149	0.145	16.720

Table 2. Powder size groups (μm)

	Groups	D10	D50	D90
Unimodal distribution	10 μm	5.3	12.5	22.6
	20 μm	16.3	22.1	29.8
	30 μm	22.1	31.3	41.8
	40 μm	25.7	36.4	48.3
Bimodal distribution	30 (73%)+10 μm	10.6	26.8	39.0
	40 (73%)+10 μm	10.7	32.7	47.4

for bimodal mixtures with a corresponding weight ratio of 27:73 which was evaluated to increase powder packing density^[30] by mixing for 2 h in a heavy-duty shaker mixer (Turbula-WAB Group, CH). Figure 1B displays powder morphology obtained at 0.8 μm per pixel, showing high sphericity in the SS316L stainless steel powder used in this work. Some surface defects and satellites were observed as well, which could be beneficial for powder flowability.

2.3. Part fabrication and printing parameters

An ExOne (North Huntingdon, PA) Innovent + binder jetting machine with 30 μm print resolution was used for the fabrication of all parts. BA005 aqueous-based binder (supplied by ExOne) was deposited which uses polyvinylpyrrolidone (PVP) polymer as a bonding agent. A total of six builds were printed corresponding to each powder size group. To evaluate and compare the mechanical strength of the unimodal and the bimodal distributions used, 31.7 mm \times 12.7 mm \times 6.35 mm bars were fabricated as per the ASTM B528-99 standard. To evaluate the sintered density in the fabricated parts (unimodal vs. bimodal), 7 mm (D) \times 20 mm (L) cylinders were printed, as shown in Figure 2.

To isolate the effects of build layout and orientation, a total of five bars and four cylinders were printed per build and placed in different locations. The bars were fabricated perpendicular to the load direction within the build platform, as shown in Figure 3.

Several studies have noted that process-related parameters affect part density and mechanical performance^[24,31]. Table 3 provides an overview of the process parameters that were utilized for the fabrication of all SS316L samples in this study. Layer thickness varied slightly across groups, as this is a variable directly related to the powder size. It is recommended that the thickness of the layers should be around 3 times the particle diameter for higher packing density and a smooth surface finish^[32]. Another parameter that slightly varied across groups was the recoat speed, which is the speed at which the hopper traverses the build while dispensing powder^[33]. It can be observed that a lower speed (mm/s) was utilized for finer particles because of the difficulty in powder dispensing due to clumping and agglomeration. In addition, bed drying time, which is the time the heat lamp takes to pass over the deposited binder for drying, was adjusted between groups due to differences in particle sizes. Observations of part bleeding and layer delamination guided the selection of bed drying time.

2.4. Post-processing

Following green part fabrication, all samples were cured in an oven at 200°C for 5 h, followed by manual

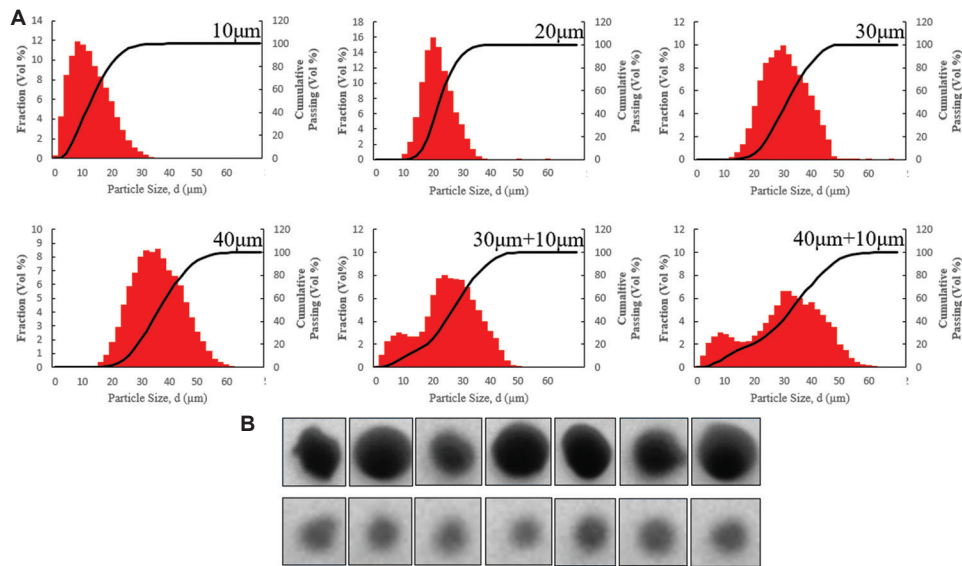


Figure 1. (A) Powder size distributions of SS316L groups. (B) Powder morphology.

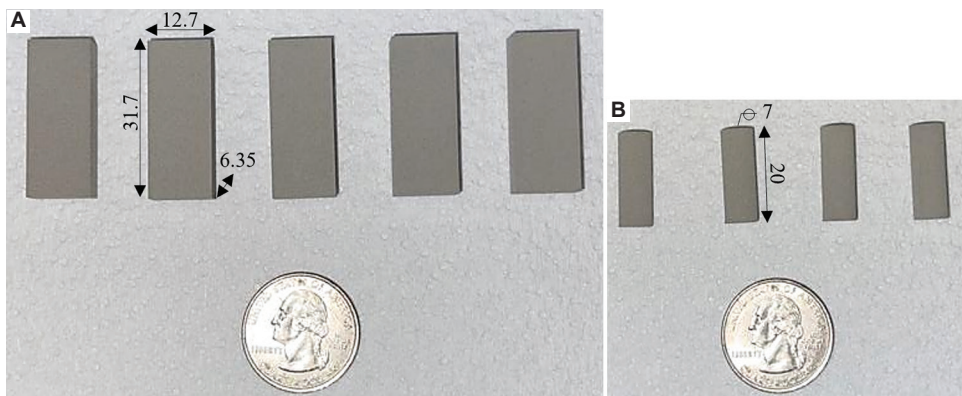


Figure 2. Example of green 10 µm group size samples. (A) Bars (mm). (B) Cylinders (mm).

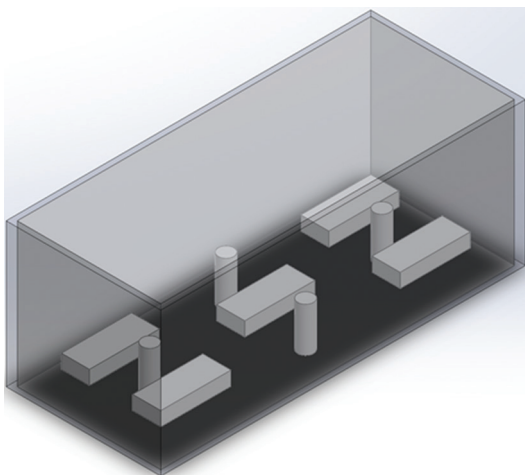


Figure 3. Build layout for each powder size group.

Table 3. Printing process parameters

Parameter	Particle size groups					
	10 µm	20 µm	30 µm	40 µm	30+10 µm	40+10 µm
Layer thickness (µm)	Ranged from 100 to 115					
Desired saturation (%)	65 in all size groups					
Rotation speed (rpm)	500 in all size groups					
Traverse speed (mm/s)	3 in all size groups					
Recoat speed (mm/s)	30	30	60	60	60	60
Bed temperature (°C)	55 in all size groups					
Bed drying time (s)	5	5	10	10	15	15

depowdering and removal from the build box. Finally, all samples were sintered in a fully inert atmosphere filled with argon gas. A tube furnace (Carbolite Gero Ltd.) was used with the following temperature profile, as shown in Figure 4: (i) 3°C/min ramp to 700°C, 60 min dwell; (ii) 3°C/min ramp to 1120°C, 140 min dwell; (iii) cool down at 3°C/min to 850°C, 90 min and to 300°C, 183 min; and (iv) cool down at 3°C/min to room temperature. A similar sinter cycle can be observed in previous SS316L binder jetting work^[24].

3. Part evaluation techniques

3.1. Sintered density

Sintered density was calculated for all cylinder samples from each group ($n = 4$) using both physical and micro-X-ray computed tomography (XCT) methods. Specimen dimensions were recorded using a digital caliper (10 μm accuracy) for the cylinder dimensions and a digital scale (0.1 mg) for weight recordings. In Equation I, the formula used for caliper density calculations is shown, where $m_{cylinder}$ is the total mass of the cylinder and $v_{cylinder}$ is the volume using the radius and height of the cylinder. This value was later divided by the theoretical density of SS316L stainless steel (8.00 g/cm³) for relative density % present in the printed part.

$$\rho_{sintered} = \frac{m_{cylinder}}{v_{cylinder}} \tag{I}$$

On collecting sintered data from all printed samples ($n = 4$ /group), a more precise calculation of density was further explored using XCT on one sample per group size. This technique was selected as it is a non-invasive tool that enables the evaluation of internal features of printed parts. A GE Vtomex L300 CT scanner with a microfocus tube was used. Scans were collected using a 250kV 40 μA X-ray beam with 10 μm voxel resolution. Raw XCT data were collected as

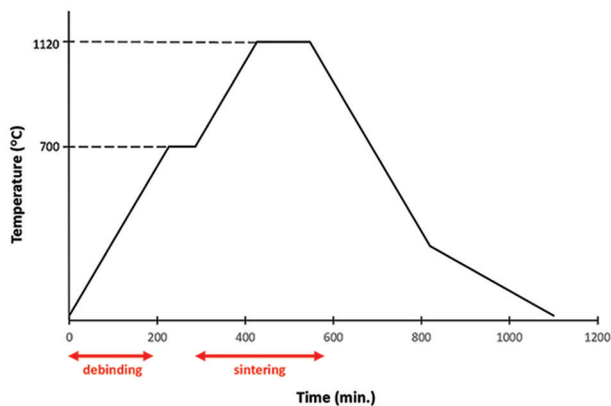


Figure 4. Time-temperature profile used for sintering SS316L samples.

16-bit tiff stack files and imported for processing into ImageJ software for image preparation and gray scale correction. AVIZO was used for the visualization and analysis of XCT data. Segmentation and thresholding of the data were performed to extract the material (SS316L) of the printed cylinder. The total volume of the solid cylinders (without accounting for porosity) was calculated using AVIZO’s internal tool. Figure 5 shows the printed cylinders from the XCT scans segmented and displayed in AVIZO. The higher part resolution achieved with 10 μm can be observed along with segmented porosity, which is shown in black.

3.2. Mechanical testing

Sintered test coupons ($n = 5$ /group size) were subjected to ultimate flexural strength (UFS) 3-point bending test as per ASTM B528-16 standard at 2.5 mm/min loading rate until complete rupture in an MTS Landmark 22 Kip servo hydraulic test. UFS and flexural modulus (FM) described in Equation II were computed based on F , L , w , t – force required to rupture, span distance, specimen width, thickness, and slope of the line tangent to the load displacement curve, respectively.

$$\sigma_{max\ flex} = \frac{3FL}{2wt^2} \tag{II}$$

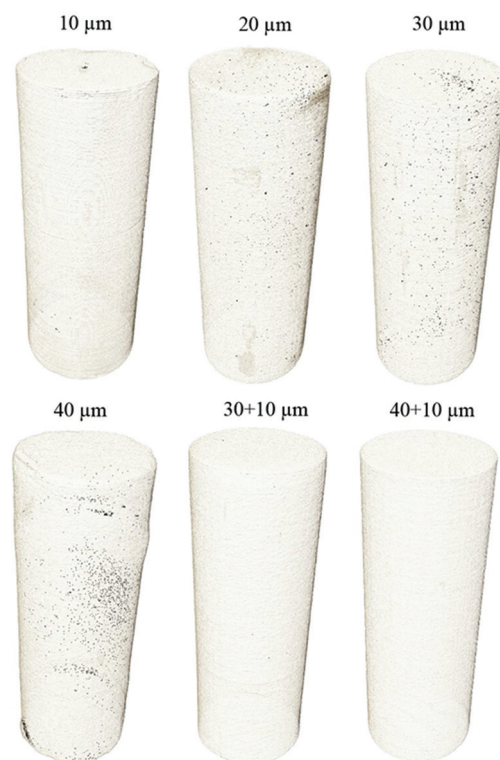


Figure 5. Pores reduced in bimodal powder size groups as observed from X-ray computed tomography results.

3.3. Statistical analysis

Statistical analysis was performed on density values and UFS to determine any statistical differences between groups. Both sintered density ($n = 4$) and UFS ($n = 5$) results were compared based on powder size groups (six groups). A Ryan-Joiner test (similar to Shapiro–Wilk) was performed ($\alpha = 0.05$) in Minitab to verify for normal distribution before Bartlett's test for equal variance. One-way analysis of variance (ANOVA; $\alpha = 0.05$) was performed, along with a Tukey multiple comparison test to compare group means. If the normality test failed, a Kruskal–Wallis non-parametric test was run in Python to evaluate the statistical difference in median values between groups. A Dunn's test, with a Bonferroni correction, was applied to identify the statistically different groups and to reduce family-wise error rate and Type I errors.

3.4. ReaxFF MD simulations

ReaxFF MD simulations are a force field-based atomistic modeling method. The smooth bond order transition for bond breaking and formation enables ReaxFF to model the solid/liquid and solid/solid chemical reactions in the binder jetting additive manufacturing process. In a previous work by the authors, the solid-liquid interactions between Cr-oxide in SS particles and binder solutions were modeled with a system that contains Cr-oxide nanoparticles, diethylene glycol, and water molecules^[25]. The simulation results provided a molecular level explanation of the strengthening mechanism from print to the sintering stages. In another study by the authors, two sizes of particles were prepared to model the bimodal particle size distribution^[26]. The particles have a Fe-Cr₂O₃ core-shell structure. The ReaxFF MD simulations were carried out at room temperature, 120°C, and 1120°C to compare the bimodal and unimodal particle size distribution regarding the chemical and physical evolution at the print, curing, and sintering stages, respectively. Rupture strengths were computed after the system reaches equilibrium at each temperature. More details regarding the simulations can be found in this paper^[34]. In this work, we compared the rupture strengths of sintered products computed with the ReaxFF potential from Gao *et al.*^[34] with experimental measured by the 3-point flexural test.

4. Results

4.1. Sintered density

Sintered density ($n = 4$ cylinders measured with calipers) corresponding to each of the six particle size distribution groups is shown in Figure 6. A visible trend within the unimodal groups is observed, showing a decrease in density as the particle sizes increase up to 40 μm . The

40 μm density was found to be 5.11% and 6.77% larger than the 20 and 30 μm groups, respectively. The 30 + 10 and 40 + 10 μm bimodal groups displayed a much higher density than any of the unimodal groups with average relative densities of 71.83% and 71.57%. In addition, the 30 + 10 and 40 + 10 μm bimodal groups showed a 20.18% and 19.74% increase in sintered density when compared to the highest density group of 10 μm unimodal powders.

The Ryan-Joiner test showed that the sintered density data presented were not normally distributed. Because of this, a Kruskal–Wallis ($\alpha = 0.05$) non-parametric test was performed, showing $P < 0.05$. This value indicated that due to the statistical difference between median values of each group, particle size distribution does have a statistical impact on the sintered density results obtained through this study. A Dunn's test with Bonferroni correction found that the 30 μm group was the only group that was statistically lower than both bimodal groups, as shown in Figure 6.

Additional density measurements were calculated using XCT data. Although minor differences can be observed in the obtained XCT densities when compared to physical measurements (8.2%), the trends are consistent with each other. For instance, the highest density was still achieved in bimodal groups at 74.82% and 76.99% followed by the unimodal 10 μm at 66.80%, as shown in Figure 7.

4.2. Three-point bending

UFS results ($n = 5$ bars) from each group, obtained from the 3-point bending test, are shown in Figure 8. A clear decreasing trend in UFS with an increase in particle size among the unimodal group can be observed, which agrees with the results found with the sintered density in Section 4.1. However, unlike the density trend reported previously, which saw a slight increase in 40 μm density compared to the 20 μm and 30 μm , a continuous decrease in UFS from 10 μm to 40 μm was observed in this study.

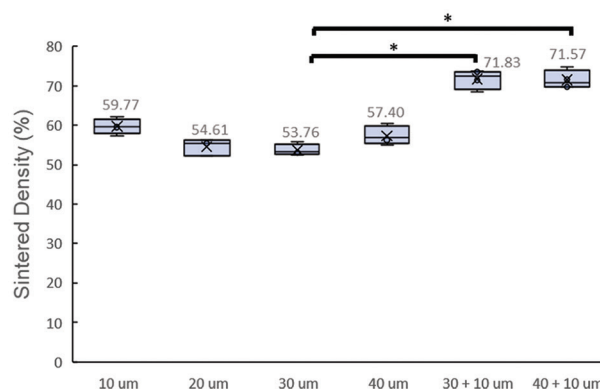


Figure 6. Sintered density values across unimodal and bimodal particle size groups. * $P = 0.01 - 0.05$.

The Ryan-Joiner test also indicated that the UFS data were not normally distributed. The Kruskal–Wallis ($\alpha = 0.05$) non-parametric test was performed. It was found that both bimodal groups were statistically higher than the 30 μm and 40 μm group, as shown in Figure 8. Due to the size limitations of the tube furnaces used for sintering, only three bars were sintered at a time. It was suspected that variation in sintering conditions both within and across particle groups could be present, as shown in Table 4. This may be an influencing factor on why statistical differences between some of the unimodal and bimodal groups were not observed, despite the 168.3% and 173.4% increase in UFS from the 10 μm to the 30 + 10 and 40 + 10 μm groups, respectively. Results gathered from samples that were sintered in the same batch were used to see the impact different sintered runs had on the UFS. As shown in Table S1 (in Supplementary File), analysis of UFS of particle size groups sintered in the same batch resulted in lower relative standard deviation (RSD). This indicates significant variations in strength between sintered groups.

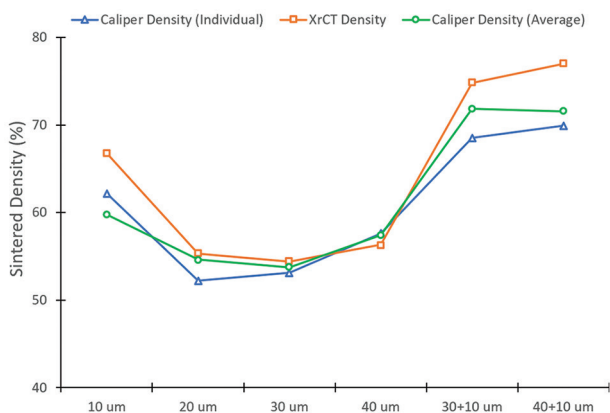


Figure 7. Relationship and trend between all particle groups with respect to X-ray computed tomography, caliper measured (individual) density, and caliper measured (average) density.

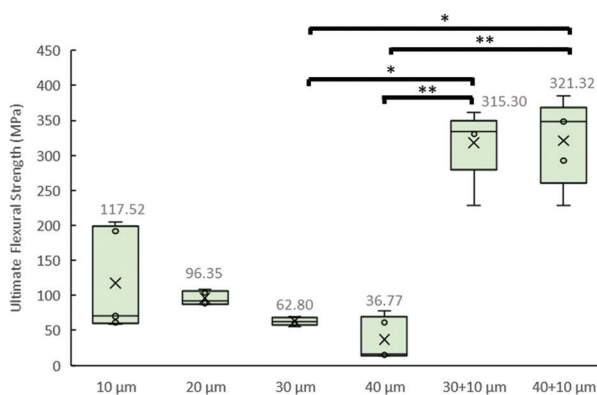


Figure 8. Ultimate flexural strength (UFS) shows that bimodal particles have higher flexural strength. * $P = 0.01 - 0.05$ and ** $P < 0.01$.

However, when both the truncated and full datasets were compared, as shown in Figure 8 and Figure S1 (in Supplementary File), a similar trend can be seen but with different statistical significance.

According to our previously reported MD simulations, the fine powders filling the interparticle voids can contribute extra bonds to connecting the coarse particles after sintering^[26]. As a result, the rupture strengths are enhanced in the bimodal particle mixture than in the unimodal particle size mixture. It should be noted that the rupture strength observed in the ReaxFF-MD simulations was improved by 40.9%, which was much lower than the >170% measured improvements demonstrated in the 3-point bending tests. This could be attributed to the lower number of fine particles in the MD simulation.

5. Discussion

Based on the findings from this study, it can be observed that bimodal distribution feedstock achieves higher density and mechanical properties for SS316L. Our work showed a statistically significant increase in sintered density with the introduction of bimodal groups when compared to unimodal distributions, which is in agreement with prior reports^[4,19,20]. The improvement in density after sintering conditions could be attributed to better filling effects that could result in more contact and necking, which is beneficial for sintering and shrinkage reduction. To the best of our knowledge, this is the first study that reports a statistically significant increase of more than 20% in sintered density in the bimodal particle size distribution.

The increase in density observed with our bimodal results aligns with Du *et al.*'s findings when studying silicon carbide in which a 5% increase in bimodal green density was observed when compared with the unimodal distributions^[25]. Du *et al.* analyzed different coarse powder fractions (%) for bimodal mixing and found the highest density values of 70 – 75% coarse particles in the mixture, which is comparable to the 73% used in this study. The appropriate selection of a coarse-to-fine ratio has been shown to impact part density. The ratio used in this study

Table 4. Summary results across particle groups

Group	Sintered density (%)			Ultimate flexural strength (MPa)		
	Mean	Std.	RSD	Mean	Std.	RSD
10 μm	59.77	1.98	3.31%	117.50	74.20	63.15%
20 μm	54.61	2.12	3.88%	96.35	9.81	10.18%
30 μm	53.76	1.43	2.66%	62.80	5.78	9.20%
40 μm	57.40	2.33	4.06%	36.80	30.80	83.70%
30+10 μm	71.83	2.47	3.44%	315.30	59.05	18.74%
40+10 μm	71.57	2.36	3.30%	321.30	61.80	19.02%

has been found to achieve high packing density in other reported studies. Bai *et al.* demonstrated that although higher sintered density was always achieved in bimodal distributions, different mixing ratios (1:3 – 1:6) would result in different values^[30].

As observed in Figure 6, a clear trend of decrease in density with an increase in particle size within unimodal groups can be observed. Similar results have been reported in the literature in other metals and ceramics^[2,35-37]. Finer particles are known to enhance the sintering process due to the initial necking when compared with coarser particles. In addition, the increase in surface energy and contact area associated with finer particles favors sinterability due to a higher particle bonding rate. In this study, density decreased with an increasing particle size up until the 40 μm group, where a slight increase in density was observed. We attribute this possible outlier to variations in sintering conditions associated with non-uniform inert atmospheres at the tail ends of the tube furnace (Figure 9A). Temperature data were tracked and gathered during each of the sinter runs, which indicated that an identical heating profile was followed for all samples. It has been reported that the density of SS316L metal injection molding parts was impacted by different gas atmospheres as well as other sintering factors^[38]. Other papers have discussed the effects of the sintering atmosphere on SS316L^[39]. As tube furnaces only have a relatively small hot zone, any minor differences in the precise placement of the samples in the alumina crucible could have caused this observation. Future studies will include real-time monitoring of gas flow rate and development of a jig to precisely repeat the placement of sintering samples within the crucible.

During the sintering stage of a binder jetting process, off-gassing takes place as the binder is evaporated from the part (debinding). A higher gas flow rate might be beneficial for uniformly carrying these chemicals out of the furnace chamber and away from the part. As shown in Figure 9, the differences between sintered runs of the same particle group have different colorations, indicating a slight difference in the gas atmosphere or flow rate. In



Figure 9. Different sinter runs for the same particle size group. *Top right bar corresponds to a different group.

addition, as shown in Figure 9A, gas flow lines are seen in only one of the samples, indicating that the possible impact sample position might have on result variability. The truncated data contain samples only sintered at the same time, resulting in much lower standard deviations, as shown in Table S1 (in Supplementary File). This is believed to be a further evidence that the higher density seen with the 40 μm cylinders might be caused by the higher amount of surface oxides. After performing data analysis on all sintered density values, the results showed no statistical difference between the 40 μm and any other unimodal groups. In summary, the bimodal groups have a higher density when compared to the unimodal groups.

In general, a higher density results in higher mechanical strength because of the detrimental impact of porosity during mechanical loading. Jost *et al.* also found that the ductility and strain at ultimate tensile strength for SS316L manufactured through powder bed fusion method were negatively impacted by porosity^[40]. Our results presented in Figure 8 agree with the claim that higher density (found in bimodal groups) corresponds to higher UFS. As previously mentioned, the 40 μm group saw a slight deviation from the observed density trend within the unimodal group. Conclusions about this phenomenon rely on the possibility of surface porosity or open porosity present with that group. Because the sintered density was calculated using physical measurements, the bulk volume (including open and closed pores) was used. Future investigations should rely on more advanced sintered density measurements, such as the Archimedes method or He pycnometry, for more precise measurement.

The surface porosity might have resulted in higher calculated density but lower strength. Reports of surface defects and roughness's impact on mechanical performance are highlighted in Masuo *et al.*'s work^[41]. Overall, no statistical difference was found between unimodal groups. The increase in UFS of bimodal particle size group when compared to unimodal groups is highly statically significant. Mechanical values presented with this work can be compared with a literature investigation where Shrestha *et al.* reported a maximum UFS of 90.10 MPa using binder jetting SS316L with similar sintering profile with only unimodal distributions.

Finally, the relative density (density calculated/theoretical density) was low (the highest sintered density achieved was around 72%) when compared to densities achieved by other studies. Based on the literature reports, sintered density in binder jetting has in some cases reached around 95% depending on the specific material and the process parameters used. A reduction in density may be a consequence of insufficient sintering conditions, such as low sintered temperatures used and possible part expansion

due to debinding caused by outgassing^[19]. A higher sinter temperature should be considered to facilitate mass transport and increase the part density^[42]. In addition, this study did not optimize binder saturation, rolling speed, and other process parameters. Based on other reported studies, higher density values have been obtained by appropriately selecting specific process and thermal parameters that would enhance the printing performance^[2,14]. Future work should focus on finding different parameters and adjusting them for density increases, as well as investigating the impact of sintering profiles and their effect on bimodal distributions as they are directly affected by powder properties and packing state.

6. Conclusions

The goal of this study was to evaluate the impact bimodal distributions in binder jetting of SS316L feedstock. Six different particle distributions, that is, four unimodal (10 μm , 20 μm , 30 μm , and 40 μm) and two bimodal (30 + 10 μm and 40 + 10 μm), were compared. An ExOne Innovent + was used to print four cylinders and five bars per particle size group. The samples were cured and sintered; cylinders were used to calculate density and bars were used for 3-point bending using weight and XCT data. Density and UFS (through 3-point bending tests) were used to compare the impact of the particle distribution. The measured UFS was compared with the MD simulations using the ReaxFF potential. Based on the results, the main conclusions are as follows:

- (i) A bimodal powder distribution is preferred over unimodal distribution in binder jetting of SS316L, for higher density and preferred mechanical performance.
- (ii) Bimodal groups were statistically denser than the unimodal groups, achieving an average increase in density of 20%.
- (iii) Bimodal groups showed a higher UFS than the unimodal groups. Both the 30 + 10 μm and 40+10 μm groups had an average increase of 170% in UFS when compared to the 10 μm group, which saw the highest UFS out of all unimodal groups. According to the MD simulations, the fine powders in the bimodal groups filling the interstitial space provided extra bonds to strengthen the sintered part.
- (iv) UFS followed the same trend observed in ReaxFF-MD simulation of bimodal powder size distribution. The improvements in mechanical strength was greater than predicted MD simulation results which could be attributed to higher number of fine particles in ASTM standard size samples when compared to MD simulations.

- (v) In the bimodal groups of this study, statistical differences in density and UFS between the groups were not observed.
- (vi) It was found that in unimodal powders, density decreases as particle size increases, despite the lack of statistical differences within the unimodal group. The 10 μm group had the highest density and was found to be the only group having statistically higher particle size compared to the 30 μm group (by 11.18%). This indicates that finer particles could result in higher density within unimodal particle sizes.
- (vii) UFS followed a similar trend to density within the unimodal group; as particle size increases, UFS decreases. The 10 μm group was found to have statistically higher UFS than the rest of the unimodal groups.
- (viii) Slight variation in the trend among observed unimodal density trend and across groups in UFS could have been caused by variability during sintering.

Future work should optimize the printing parameters of the bimodal groups to achieve the highest possible density and UFS. In addition to different sintering profiles and sample position, the effects of gas flow rate during sintering should be further investigated. Finally, the effect of powder binder interaction in bimodal distributions could be investigated both through MD simulation and experimental efforts, including in-process monitoring.

Acknowledgments

The authors acknowledge the support from the ExOne Company, The Pennsylvania State University, Tim Stecko, and Verder Scientific for their assistance.

Funding

This work was funded by NSF CAREER CMMI #1944120 and partially by Manufacturing PA program.

Conflict of interest

There are no conflicts of interest to declare.

Author contributions

Conceptualization: Ana Paula Clares, Adri C.T. van Duin, and Guha Manogharan

Formal analysis: Ana Paula Clares and Ryan Stebbins

Funding acquisition: Guha Manogharan

Investigation: Ana Paula Clares

Methodology: Ana Paula Clares

Project Administration: Guha Manogharan

Resources: Guha Manogharan

Supervision: Adri C.T. van Duin and Guha Manogharan

Writing – original draft: Ana Paula Clares, Yawei Gao, and Ryan Stebbins

Writing – review & editing: Adri C.T. van Duin and Guha Manogharan.

References

1. Mirzababaei S, Pasebani S, 2019, A review on binder jet additive manufacturing of 316L stainless steel. *J Manuf Mater Process*, 3: 82.
<https://doi.org/10.3390/JMMP3030082>
2. Bai Y, Williams C, 2015, An exploration of binder jetting of copper. *Rapid Prototyp J*, 21: 177–185.
<https://doi.org/10.1108/RPJ-12-2014-0180>
3. Liravi F, Vlasea M, 2018, Powder bed binder jetting additive manufacturing of silicone structures. *Addit Manuf*, 21: 112–124.
<https://doi.org/10.1016/j.addma.2018.02.017>
4. Sama SR, Badamo T, Manogharan G, 2020, Case studies on integrating 3D sand-printing technology into the production portfolio of a sand-casting foundry. *Int J Met*, 14: 12–24.
<https://doi.org/10.1007/s40962-019-00340-1>
5. Mariani M, Beltrami R, Brusa P, *et al.*, 2021, 3D printing of fine alumina powders by binder jetting. *J Eur Ceram Soc*, 41: 5307–5315.
<https://doi.org/10.1016/j.jeurceramsoc.2021.04.006>
6. Cramer CL, Aguirre TG, Wieber NR, *et al.*, 2020, Binder jet printed WC infiltrated with pre-made melt of WC and Co. *Int J Refract Met Hard Mater*, 87: 105137.
<https://doi.org/10.1016/j.jirmhm.2019.105137>
7. Manogharan G, Kioko M, Linkous C, 2015, Binder jetting: A novel solid oxide fuel-cell fabrication process and evaluation. *JOM*, 67: 660–667.
<https://doi.org/10.1007/s11837-015-1296-9>
8. Ke D, Bose S, 2018, Effects of pore distribution and chemistry on physical, mechanical, and biological properties of tricalcium phosphate scaffolds by binder-jet 3D printing. *Addit Manuf*, 22: 111–117.
<https://doi.org/10.1016/j.addma.2018.04.020>
9. Martinez D, Bate C, Manogharan GP, 2020, Towards functionally graded sand molds for metal casting: Engineering thermo-mechanical properties using 3D sand printing. *JOM*, 72: 1340–1354.
<https://doi.org/10.1007/s11837-019-03975-x>
10. Xia M, Sanjayan J, 2016, Method of formulating geopolymer for 3D printing for construction applications. *Mater Des*, 110: 382–390.
<https://doi.org/10.1016/j.matdes.2016.07.136>
11. Rojas-Nastrucci EA, Nussbaum JT, Crane NB, *et al.*, 2017, Ka-band characterization of binder jetting for 3-D printing of metallic rectangular waveguide circuits and antennas. *IEEE Trans Microw Theory Tech*, 65: 3099–3108.
<https://doi.org/10.1109/TMTT.2017.2730839>
12. Lecis N, Mariani M, Beltrami R, *et al.*, 2021, Effects of process parameters, debinding and sintering on the microstructure of 316L stainless steel produced by binder jetting. *Mater Sci Eng A*, 828: 142108.
<https://doi.org/10.1016/J.MSEA.2021.142108>
13. Li M, Du W, Elwany A, *et al.*, 2019, Binder Jetting Additive Manufacturing of Metals: A Literature Review. Vol. 1. In: ASME 2019 14th International Manufacturing Science and Engineering Conference.
<https://doi.org/10.1115/MSEC2019-2994>
14. Bai Y, Wagner G, Williams CB, 2015, Effect of bimodal powder mixture on powder packing density and sintered density in binder jetting of metals: In Annual International Solid Freeform Fabrication Symposium (2015), 62.
15. Li M, Du W, Elwany A, *et al.*, 2020, Metal binder jetting additive manufacturing: A literature review. *J Manuf Sci Eng Trans ASME*, 142: 090801.
<https://doi.org/10.1115/1.4047430/1084395>
16. Gibson I, Rosen D, Stucker B, *et al.*, 2020, Binder jetting. In: *Additive Manufacturing Technologies.*, Champaign: Springer International Publishing, p237–252.
17. Ziaee M, Tridas EM, Crane NB, 2017, Binder-jet printing of fine stainless steel powder with varied final density. *JOM*, 69: 592–596.
<https://doi.org/10.1007/s11837-016-2177-6>
18. Meenashisundaram GK, Xu Z, Nai ML, *et al.*, 2020, Binder jetting additive manufacturing of high porosity 316L stainless steel metal foams. *Materials*, 13: 3744.
<https://doi.org/10.3390/MA13173744>
19. Vogt J, Friedrich H, Stepanyan M, *et al.*, 2021, Improved green and sintered density of alumina parts fabricated by binder jetting and subsequent slurry infiltration. *Prog Addit Manuf*, 7: 161–171.
<https://doi.org/10.1007/S40964-021-00222-1>
20. Porter Q, Pei Z, Ma C, 2022, Binder jetting and infiltration of metal matrix nanocomposites. *J Manuf Sci Eng*, 144: 074502.
<https://doi.org/10.1115/1.4053156>
21. Kumar AY, Bai Y, Eklund A, *et al.*, 2018, The effects of hot isostatic pressing on parts fabricated by binder jetting additive manufacturing. *Addit Manuf*, 24: 115–124.
<https://doi.org/10.1016/J.ADDMA.2018.09.021>
22. Kumar A, Bai Y, Eklund A, *et al.*, 2017, Effects of hot isostatic

- pressing on copper parts fabricated via binder jetting. *Procedia Manuf*, 10: 935–944.
<https://doi.org/10.1016/J.PROMFG.2017.07.084>
23. Dahmen T, Henriksen NG, Dahl KV, *et al.*, 2021, Densification, microstructure, and mechanical properties of heat-treated MAR-M247 fabricated by binder jetting. *Addit Manuf*, 39: 101912.
<https://doi.org/10.1016/J.ADDMA.2021.101912>
 24. Shrestha S, Manogharan G, 2017, Optimization of binder jetting using taguchi method. *JOM*, 69: 491–497.
<https://doi.org/10.1007/s11837-016-2231-4>
 25. Du W, Singh M, Singh D, 2020, Binder jetting additive manufacturing of silicon carbide ceramics: Development of bimodal powder feedstocks by modeling and experimental methods. *Ceram Int*, 46: 19701–19707.
<https://doi.org/10.1016/j.ceramint.2020.04.098>
 26. Du W, Ren X, Chen Y, *et al.*, 2018, Model Guided Mixing of Ceramic Powders with Graded Particle Sizes in Binder Jetting Additive Manufacturing. Vol. 1. In: ASME 2018 13th International Manufacturing Science and Engineering Conference. p9.
<https://doi.org/10.1115/MSEC2018-6651>
 27. Du W, Roa J, Hong J, *et al.*, 2021, Binder jetting additive manufacturing: Effect of particle size distribution on density. *J Manuf Sci Eng*, 143: 091002.
<https://doi.org/10.1115/1.4050306>
 28. Clares AP, Manogharan G, (2021), Discrete-element Simulation of Powder Spreading Process in Binder Jetting, and the Effects of Powder Size. In: ASME 2021 16th International Manufacturing Science and Engineering Conference.
 29. Standard, ASTM, 2012, ISO/ASTM 52900: 2015 Additive manufacturing-General principles-terminology. ASTM F2792-10e1.
 30. Bai Y, Wagner G, Williams CB, 2017, Effect of particle size distribution on powder packing and sintering in binder jetting additive manufacturing of metals. *J Manuf Sci Eng Trans ASME*, 139: 081019.
<https://doi.org/10.1115/1.4036640>
 31. Chen H, Zhao YF, 2016, Process parameters optimization for improving surface quality and manufacturing accuracy of binder jetting additive manufacturing process. *Rapid Prototyp J*, 22: 527–538.
<https://doi.org/10.1108/RPJ-11-2014-0149/FULL/PDF>
 32. Utela B, Storti D, Anderson R, *et al.*, 2008, A review of process development steps for new material systems in three dimensional printing (3DP). *J Manuf Process*, 10: 96–104.
<https://doi.org/10.1016/J.JMAPRO.2009.03.002>
 33. Mostafaei A, Elliott AM, Barnes JE, *et al.*, 2020, Binder jet 3D printing-Process parameters, materials, properties, and challenges. *Prog Mater Sci*, 119: 100707.
<https://doi.org/10.1016/j.pmatsci.2020.100707>
 34. Gao Y, Clares AP, Manogharan G, *et al.*, 2022, A reactive molecular dynamics study of bi-modal particle size distribution in binder-jetting additive manufacturing using stainless-steel powders. *Phys Chem Chem Phys*, 24: 11603–11615.
<https://doi.org/10.1039/D2CP00630H>
 35. Miyajima H, Momenzadeh N, Yang L, 2019, Effect of powder characteristics on parts fabricated via binder jetting process. *Rapid Prototyp J*, 25: 332–342.
<https://doi.org/10.1108/RPJ-03-2018-0069/FULL/PDF>
 36. Verlee B, Dormal T, Lecomte-Beckers J, 2013, Density and porosity control of sintered 316L stainless steel parts produced by additive manufacturing. *Powder Metallurgy*, 55: 260–267.
<https://doi.org/10.1179/0032589912Z.00000000082>
 37. Miao G, Du W, Moghadasi M, *et al.*, 2020, Ceramic binder jetting additive manufacturing: Effects of granulation on properties of feedstock powder and printed and sintered parts. *Addit Manuf*, 36: 101542.
<https://doi.org/10.1016/j.addma.2020.101542>
 38. Ji CH, Loh NH, Khor KA, *et al.*, 2001, Sintering study of 316L stainless steel metal injection molding parts using Taguchi method: Final density. *Mater Sci Eng A*, 311: 74–82.
[https://doi.org/10.1016/S0921-5093\(01\)00942-X](https://doi.org/10.1016/S0921-5093(01)00942-X)
 39. Sridhar TM, Mudali UK, Subbaiyan M, 2003, Sintering atmosphere and temperature effects on hydroxyapatite coated type 316L stainless steel. *Corros Sci*, 45: 2337–2359.
[https://doi.org/10.1016/S0010-938X\(03\)00063-5](https://doi.org/10.1016/S0010-938X(03)00063-5)
 40. Jost EW, Miers JC, Robbins A, *et al.*, 2021, Effects of spatial energy distribution-induced porosity on mechanical properties of laser powder bed fusion 316L stainless steel. *Addit Manuf*, 39: 101875.
<https://doi.org/10.1016/J.ADDMA.2021.101875>
 41. Masuo H, Tanaka Y, Morokoshi S, *et al.*, 2017, Effects of defects, surface roughness and HIP on fatigue strength of Ti-6Al-4V manufactured by additive manufacturing. *Procedia Struct Integr*, 7: 19–26.
<https://doi.org/10.1016/J.PROSTR.2017.11.055>
 42. Du W, Ren X, Pei Z, *et al.*, 2020, Ceramic binder jetting additive manufacturing: a literature review on density. *J Manuf Sci Eng*, 142: 040801.
<https://doi.org/10.1115/1.4046248>